A Journal of the Gesellschaft Deutscher Chemiker

Angewandte International Edition

GDCh

Chemie

www.angewandte.org

Accepted Article

Title: Steam-Induced Coarsening of Single-Unit-Cell MFI Zeolite Nanosheets and its Effect on External Surface Brønsted Acid Catalysis

Authors: Yasmine Guefrachi, Geetu Sharma, Dandan Xu, Gaurav Kumar, Katherine Vinter, Omar Abdelrahman, Xinyu Li, Saeed Alhassan, Paul Dauenhauer, Alexandra Navrotsky, Wei Zhang, and Michael Tsapatsis

To be cited as: *Angew. Chem. Int. Ed.* 10.1002/anie.202000395
Angew. Chem. 10.1002/ange.202000395

Link to VoR: http://dx.doi.org/10.1002/anie.202000395
http://dx.doi.org/10.1002/ange.202000395

WILEY-VCH

10.1002/anie.202000395

WILEY-VCH

RESEARCH ARTICLE

Steam-Induced Coarsening of Single-Unit-Cell MFI Zeolite Nanosheets and its Effect on External Surface Brønsted Acid Catalysis

Yasmine Guefrachi,[a] Geetu Sharma,[b] Dandan Xu,[a] Gaurav Kumar,[a] Katherine P. Vinter,[a] Omar A. Abdelrahman,[a] Xinyu Li,[a] Saeed Alhassan,[c] Paul J. Dauenhauer,[a] Alexandra Navrotsky,[b] Wei Zhang,[d],[e] and Michael Tsapatsis*[a],[f],[g]

[a] Y. Guefrachi, D. Xu, G. Kumar, K. P. Vinter, O. A. Abdelrahman, X. Li, Prof. P. J. Dauenhauer, Prof. M. Tsapatsis
Department of Chemical Engineering and Materials Science
University of Minnesota
421 Washington Avenue SE, Minneapolis, MN 55455 (USA)
[*] E-mail: tsapatsis@jhu.edu
[b] Dr. G. Sharma, Prof. A. Navrotsky
Peter A. Rock Thermochemistry Laboratory, NEAT-ORU
University of California Davis
Davis, CA 95616 (USA)
[c] Prof. S. Alhassan
Department of Chemical Engineering
Khalifa University of Science and Technology
Habshan Building, Sas Al Nakhl Campus, Abu Dhabi (UAE)
[d] Prof. W. Zhang
Department of Diagnostic and Biological Sciences
University of Minnesota
515 Delaware St SE, Minneapolis, MN 55455 (USA)
[e] Characterization Facility
University of Minnesota
312 Church St, Minneapolis, MN 55455 (USA)
[f] Department of Chemical and Biomolecular Engineering and Institute for NanoBioTechnology
Johns Hopkins University
3400 N. Charles Street, Baltimore, MD 21218 (USA)
[g] Applied Physics Laboratory
Johns Hopkins University
11100 Johns Hopkins Road, Laurel, MD 20723 (USA)

Supporting information for this article is given via a link at the end of the document.

Abstract: Commonly used methods to assess crystallinity, micro-/mesoporosity, Brønsted acid site density and distribution (in micro- vs. mesopores), and catalytic activity suggest nearly invariant structure and function for aluminosilicate zeolite MFI two-dimensional nanosheets before and after superheated steam treatment. Yet, pronounced reaction rate decrease for benzyl alcohol alkylation with mesitylene, a reaction that cannot take place in the zeolite micropores, is observed. Transmission electron microscopy images reveal pronounced changes in nanosheet thickness, aspect ratio and roughness indicating that nanosheet coarsening and the associated changes in the external (mesoporous) surface structure are responsible for the changes in the external surface catalytic activity for benzyl alcohol alkylation with mesitylene. It is demonstrated that superheated steam treatment of hierarchical zeolites can be used to alter nanosheet morphology and regulate external surface catalytic activity while preserving micro- and mesoporosity, and micropore reaction rates.

Introduction

During their use, zeolites are typically exposed to hydrothermal treatments which may alter their structure at the atomic to the nanometer scale with desirable or undesirable effects on performance.[1–14] Understanding and controlling the water vapor-induced structural rearrangements[15–23] at the nanometer (single-unit-cell) level is of particular significance for two-dimensional (2D) zeolites[24,25] and thicker nanosheets[26] that constitute an emerging class of catalysts, adsorbents and membranes.[27–34] Here, we demonstrate that an all-silica single-unit-cell meso/microporous MFI-type zeolite (SPP: self-pillared pentasil)[35–38] retains its crystallinity and micro- and mesoporosity under steaming at 350 °C, while small but detectable changes take place in the content of silanol groups and the enthalpy of transition ($\Delta H_{Transition}$) relative to α-quartz (the most stable polymorph of silica under ambient conditions). Electron microscopy reveals major changes in the nanosheet dimensions: increase in thickness along the *b*-direction (straight pore channels) and reduction of basal ((010) plane) dimensions along the *c*-direction. Implications of these changes are shown to be significant for the catalytic performance of aluminosilicate SPP providing a method for controlling external surface catalytic activity without interfering with catalysis in the micropores.

Results and Discussion

All-silica SPP was synthesized based on the reported procedure[35] and its evolution was monitored during exposure to an equimolar mixture of superheated steam and nitrogen at 350

10.1002/anie.202000395

°C for up to 30 days (Section SI and Figure S1 in the Supporting Information).

The morphology of calcined SPP (before steaming) has been described in detail elsewhere.[35,36] For completeness, we provide TEM images in Figure S2a-g and a detailed discussion in Section SII in the Supporting Information. Also, a 3D view perspective of the starting calcined SPP is obtained through the aligned tilt-series displayed in Multimedia S1 in the Supporting Information. Briefly, SPP consists of intergrown nanosheets that are 2 nm-thick (i.e., one unit-cell-thick) along their *b*-axis and ca. 20x50 nm^2 in their basal plane. This is illustrated by the representative images obtained by 3D TEM tomography[39–41] shown in Figure 1. The 2D TEM images collected in the tilt-series are used along with a numerical algorithm (IMOD software package, Version 4.9, University of Colorado, Boulder, CO, USA)[42] to reconstruct the real space structure and map it into a 3D tomogram. The generated tomograms are presented as sequential numerical cross-sectional images (0.52 nm-thick) made along a certain zone axis. These cross-sections are regarded as virtual slices obtained from running a sharp virtual knife through the 3D reconstructed model. Figure 1 confirms the 2D uniformity of the domains. They are single-unit-cell throughout the length of [010].

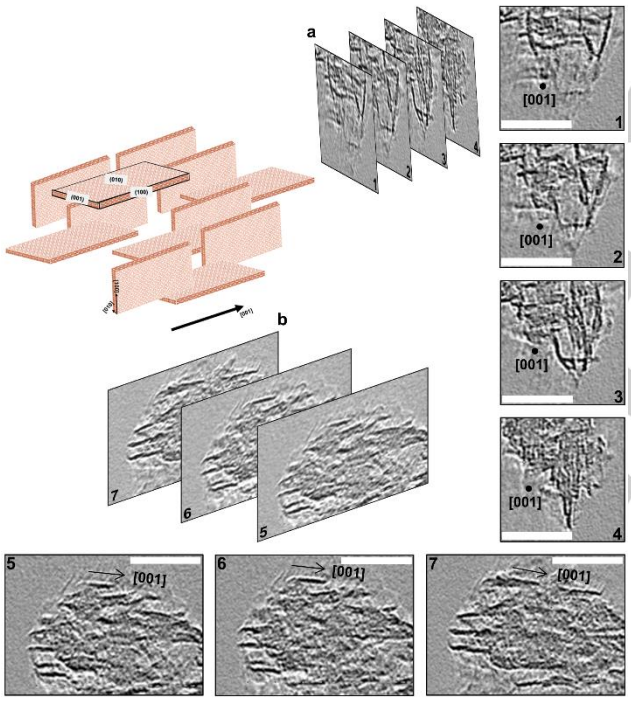

Figure 1. 3D TEM tomography of calcined SPP with a schematic representation of a portion of SPP particle consisting of intergrown single-unit-cell-thick MFI nanosheets. a) Sequential (numbered 1-4) cross-sectional images along [001]. b) Sequential (numbered 5-7) cross-sectional images along [100]/[010]. Thickness of each image is 0.52 nm. Scale bars are 50 nm.

SPP exposed to steam loses the characteristic thin dimension of the MFI nanosheets along the *b*-axis. TEM images are presented in Figure S2h-n and discussed in Section SII in the Supporting Information. Representative tomograms are presented in Figure 2. The observed changes in the relative dimensions of SPP nanosheets upon steaming are quantified by determining the dimensions of one hundred domains in the starting and the 7-day steamed SPP (Figure 3a). The dimensions along the *b*-axis and the *a*-axis were measured using the tomogram cross-sections made along the [001] zone axis, while the length along the *c*-axis was measured using the cross-sections made along the common [100]/[010] zone axes. The relative changes in the dimensions of the domains are evident by inspection of the corresponding histograms shown in Figure 3a. Despite possible deviations of the domain dimensions from a Gaussian distribution, we adapt it here in order to estimate representative mean values. The thickness along *b* evolved from 2.1 nm (a single MFI unit-cell dimension along *b*) to an average thickness of 8.5 nm (ca. four-unit-cell). The average length along the *a*-axis before and after steam treatment was found to be 17.6 nm and 14.5 nm, respectively, with the Gaussian fits to the length distributions nearly indistinguishable. The average length along the *c*-axis becomes significantly shorter (22.5 nm from 44.6 nm) with a narrower length distribution. This analysis establishes that the main characteristic of the evolution during steam treatment is thickening of the nanosheets perpendicular to their basal plane (along the *b*-axis) and shortening of the basal dimensions mostly along the *c*-axis. The TEM images show that the evolved domains adopt curved edges, exhibit increased roughness and become more globular compared to the well-defined 2D MFI nanosheets in SPP before steam treatment. Apparently, local rearrangements of silica within individual SPP particles are responsible for these changes and the preservation of the intergrown architecture. The aligned tilt-series of steamed SPP showing the above described morphology in 3D is shown in Multimedia S2.

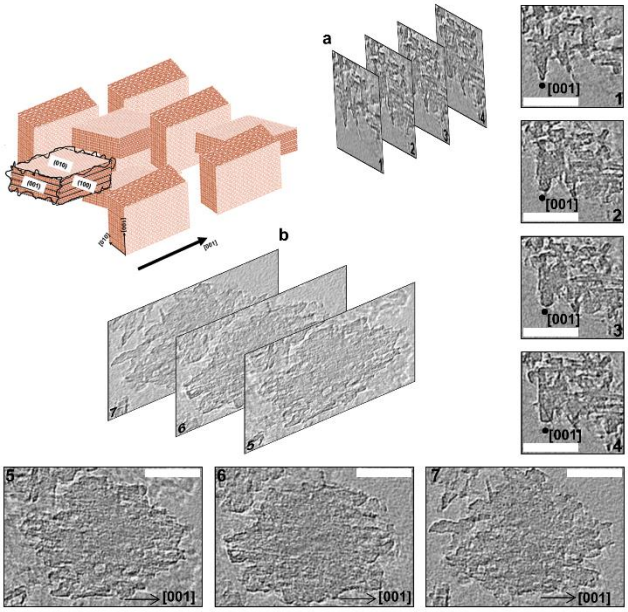

Figure 2. 3D TEM tomography of 7-day steamed SPP with a schematic representation of a portion of a coarsened SPP particle. a) Sequential (numbered 1-4) cross-sectional images along [001]. b) Sequential (numbered 5-7) cross-sectional images along [100]/[010]. Thickness of each image is 0.52 nm. Scale bars are 50 nm.

SPP evolution during steaming was followed by the thickening along the *b*-direction (using TEM images down the *c*-axis) and was found to proceed faster at the beginning and very

10.1002/anie.202000395
WILEY-VCH

RESEARCH ARTICLE

slow after 5.25 days of steaming (Figure 3b); for example, the thickness of the 7-day steamed SPP sheets shown in Figure 3d is comparable to that of the 11-day steamed SPP in Figure 3e.

Despite the major morphological changes described above, steamed SPP exhibited indistinguishable X-ray diffraction (XRD) patterns compared to the starting material irrespective of the treatment duration (Figure 4a). This finding confirms retention of crystallinity (i.e., no evidence of amorphization) and preservation of the crystallographic alignment of the domains within the individual SPP particles, (i.e., preservation of the original 90° intergrown architecture which coherently connects all individual domains aligned as parts of a single crystal). Argon (Ar) physisorption isotherms also remain invariant upon steam treatment (Figure 4b) revealing that although there are drastic changes in the domain morphology, the microporosity and mesoporosity within SPP particles remain unaltered (Figure S3). Apparently, any increase in microporous volume and decrease in mesoporosity due to the zeolite domain thickening along [010] is exactly offset by the contraction experienced mostly along [001] and somewhat along [100] (Figure 3a). Use of the invariant XRD and Ar physisorption data as criteria to monitor the effect of steam treatment would have mistakenly implied stability of 2D nanosheets in SPP, whereas the TEM and 3D tomography results discussed above, demonstrate that the nanosheets lose their 2D (i.e., single-unit-cell) morphology.

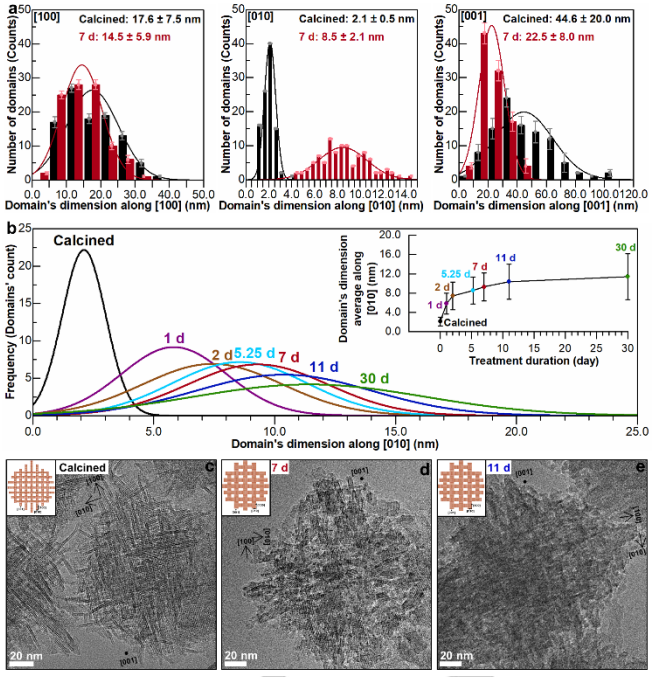

Figure 3. Evolution of domains in steamed SPP. a) Dimensions of one hundred MFI domains of calcined SPP (black) and 7-day steamed SPP (red) determined using 3D TEM tomography along [100], [010] and [001] fitted to Gaussian distributions. b) Gaussian distributions of nanosheet thickness along the *b*-axis of one hundred MFI domains of calcined SPP (black), 1- (purple), 2- (brown), 5.25- (arctic), 7- (red), 11- (blue) and 30-day (green) steamed SPP as determined by TEM; inset is the time evolution of nanosheet thickness along [010]. The black line is a tracking line for better visualization. c) Single-unit-cell SPP particle viewed down [001]. d) 7-day steamed coarsened SPP particle viewed down [001]. e) 11-day steamed coarsened SPP particle viewed down [001]; insets in c-e are idealized schematics of the house-of-cards architecture.

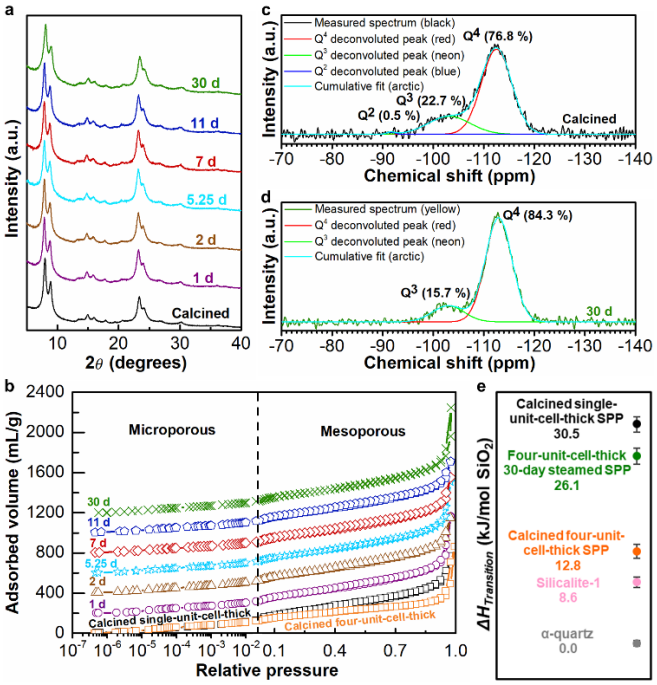

Figure 4. Evolution of crystallinity, porosity and silica connectivity in steamed SPP. a) Powder XRD patterns of calcined single-unit-cell SPP (black), 1- (purple), 2- (brown), 5.25- (arctic), 7- (red), 11- (blue) and 30-day (green) steamed SPP as measured under the same conditions and compared in the same vertical scale. b) Ar adsorption and desorption isotherms of calcined single-unit-cell SPP (black), 1- (purple), 2- (brown), 5.25- (arctic), 7- (red), 11- (blue) and 30-day (green) steamed SPP and calcined (directly-synthesized) four-unit-cell SPP (orange). The isotherms of the calcined single-unit-cell SPP and the steamed SPP are identical; they are offset by 200, 400, 600, 800, 1000 and 1200 mL/g, respectively for better visualization. c) Solid-state ^{29}Si MAS NMR spectrum of calcined single-unit-cell SPP. Shown are the measured spectrum (black), Q^4 (red), Q^3 (neon) and Q^2 (blue) deconvoluted peaks fitted to Gaussian functions and the cumulative fit (arctic). d) Solid-state ^{29}Si MAS NMR spectrum of 30-day steamed SPP. Shown are the measured spectrum (green), Q^4 (red), and Q^3 (neon) deconvoluted peaks fitted to Gaussian functions and the cumulative fit (arctic). e) Enthalpy of transition relative to α-quartz at 25 °C ($\Delta H_{Transition}$): $\Delta H_{Transition}$ of starting calcined single-unit-cell SPP (black) = 30.45 ± 1.07 kJ/mol SiO_2, $\Delta H_{Transition}$ of four-unit-cell 30-day steamed SPP (green) = 26.09 ± 1.10 kJ/mol SiO_2, $\Delta H_{Transition}$ of four-unit-cell (directly-synthesized) SPP (orange) = 12.82 ± 0.93 kJ/mol SiO_2, $\Delta H_{Transition}$ of silicalite-1[45] (pink) = 8.56 ± 0.72 kJ/mol SiO_2 and $\Delta H_{Transition}$ of α-quartz[45] (grey) = 0.00 ± 0.40 kJ/mol SiO_2.

Changes, albeit small, after steam treatment are also evident in the ^{29}Si Magic Angle Spinning (MAS) NMR spectrum shown in Figure 4d. A comparison of the corresponding spectra before and after steam treatment, shown in Figure 4c,d, shows a clear but small (ca.10 %) increase of the Q^4 fraction, which can be attributed to defect (e.g., Q^2 and Q^3 sites at nanosheets edges, internal silanol defects, etc.) elimination and/or differences in surface density of silanol groups among the expressed crystal facets within SPP particles.[43,44] Consistent with earlier work,[45] oxide melt drop solution calorimetry indicates that the reduced silanol group density in steamed SPP is associated with an enthalpic stabilization. Figure 4e shows the $\Delta H_{Transition}$ for the starting single-unit-cell SPP and the steamed SPP along with the reported value for conventional silicalite-1.[45] Among the listed materials, SPP consisting of single-unit-cell nanosheets is the least energetically stable. It is destabilized by an enthalpy of 30.5 kJ/mol SiO_2 relative to α-quartz, while the 30-day steamed SPP is 26.1 kJ/mol SiO_2 less stable in enthalpy than α-quartz. Although

more enthalpically stable than the starting single-unit-cell SPP, steamed SPP remains far from the microporous most stable zeolitic form of the MFI topology, silicalite-1,[46] which was found to be only 8.6 kJ/mol SiO_2 less stable than α-quartz.[45]

The marginal enthalpic stabilization and consistently small changes in Q^n distribution, as well as the invariant XRD and Ar physisorption data, are not representative of the pronounced coarsening of the single-unit-cell domains within SPP caused by steam treatment.

In order for the observed coarsening to take place, silica bonds should break and reform and silicate surface species should diffuse along the rearranging surfaces. It is remarkable that these processes do not lead to the creation of amorphous or dense silicates and that the evolution ceases while the material remains enthalpically destabilized retaining its original microporosity and mesoporosity.

A dynamic picture of the zeolite crystal in the presence of superheated steam is emerging from these observations; the crystalline framework rearranges itself, on timescales similar to those typically encountered in catalyst operation, to reach a kinetically or entropically stabilized hierarchical structure with similar initial crystallinity, meso- and microporosity. Although the zeolite domains within SPP particles remain nanosized, they do not retain their 2D (single-unit-cell-thick) morphology. This morphological evolution of domains within SPP yields a new material and offers a new degree of freedom in controlling their properties.

We first contrast (i) steamed SPP, coarsened from single-unit-cell to become four-unit-cell-thick along [010] with (ii) untreated, i.e., directly-synthesized SPP, composed of four-unit-cell-thick nanosheets. Synthesis of the later is described in Section SI in the Supporting Information. Figure S4 shows TEM images that reveal significant differences; the directly-synthesized material consists of relatively densely-packed high-aspect-ratio nanosheets compared to more globular and less densely-packed domains in steamed SPP. Consistent with the observed SPP particle morphologies, the Ar physisorption isotherm of material (ii) (included in Figure 4b) shows a slightly higher adsorbed volume in the microporous range and a significantly lower one in the mesoporous range relative to that of material (i). Moreover, the less mesoporous four-unit-cell directly-synthesized SPP (material (ii)) is found to be much more enthalpically stabilized compared to material (i) (with $\Delta H_{Transition}$ of 12.8 kJ/mol SiO_2 vs. 26.1 kJ/mol SiO_2, as shown in Figure 4e). These findings suggest that the two materials, despite having the same characteristic length along the *b*-axis, have very different hierarchical architecture: the directly-synthesized material (ii) is less mesoporous with its high-aspect-ratio intergrown nanosheets exposing well-defined crystal facets (dominated by (010) surfaces), while the steam-coarsened SPP material (i) has higher mesoporosity with lower aspect ratio nanosheets exhibiting not as well-defined faces with increased roughness.

We examine next the effect of steam treatment on two aluminosilicate SPP catalysts with Si/Al ratio of ca. 120 and 100, one with thin (3.8 ± 1.7 nm along *b*) and one with thicker (7.3 ± 2.6 nm) intergrown nanosheets, which after steam treatment evolve to (7.5 ± 2.3 nm) and (9.2 ± 2.1 nm), respectively. As with the all-silica SPP, these morphological changes take place while XRD patterns and Ar physisorption isotherms remain invariant (Figure S5), and only small changes are observed by ^{29}Si and ^{27}Al MAS NMR (Figure S6). In Table 1, we include total Brønsted acid site densities of these four aluminosilicate SPP catalysts (thin-SPP, steamed-thin-SPP, thick-SPP and steamed-thick-SPP, denoted as SPP, s-SPP, tk-SPP, s-tk-SPP, respectively) as measured by the Hofmann elimination of *tert*-butylamine via reactive gas chromatography,[47] along with external Brønsted acid site fraction (f_{ext}) determined by ethanol dehydration using 2,6-di-*tert*-butylpyridine (DTBP) as a titrant of external Brønsted acid sites.[48–50] Total acid site densities change by less than 25 % upon steam treatment indicating moderate dealumination. Turn over frequency (TOF) of ethanol dehydration to diethyl ether in the absence of DTBP remains similar across all materials tested indicating that the nature of active sites as probed by this reaction remains unaltered (Table S3). The fraction of external sites of SPP (47 %) is much higher than that of tk-SPP (21 %) and both conform with the expected (developed earlier based on geometric arguments)[37] dependence on high-aspect-ratio nanosheet half-thickness along *b* (x_p) shown in Figure 5a. The external Brønsted acid site fractions of SPP and tk-SPP increase upon steam treatment from 47 % to 51 % and from 21 % to 27 %, respectively. This nearly invariant f_{ext} is consistent with the observed preservation of micro- and mesoporosity upon steam-induced coarsening of SPP.

Although ethanol dehydration indicates unaltered catalytic activity upon steam treatment, a drastically different outcome is observed when we use benzyl alcohol etherification to dibenzyl ether and benzyl alcohol alkylation with mesitylene as probe reactions under the reaction conditions specified in Section SI in the Supporting Information. The first reaction takes place both in micro- and mesopores of SPP, while alkylation can only take place in the mesopores (external surfaces of nanosheets).[37,51,52] In earlier work, we developed a reaction-diffusion mathematical model (Section SIII in the Supporting Information) for these reactions and obtained the reaction rate and equilibrium constants that determine the observed etherification and alkylation rates.[37] This was accomplished using experimental data from directly-synthesized SPP catalysts with different nanosheet thicknesses. The alkylation and etherification rates can be written as shown in Eq. S1 and Eq. S2 in the Supporting Information, respectively, while the selectivity $S_{B/P}$ (etherification rate over alkylation rate) is given in Eq. S3 in the Supporting Information, which with the parameters of Table S2 becomes Eq. S4 in the Supporting Information that is plotted in Figure 5b.[37]

We have shown that the etherification rate in SPP is free of micropore diffusion effects (i.e., the micropore effectiveness factor η_m is ca. 1) for nanosheet thicknesses below ca. 20 nm, while diffusion limitations emerge for crystals with larger characteristic diffusion lengths.[37] As discussed in Xu et al.[37] and shown in Figure 5b for the SPP catalysts (points 1, 2 and 3), etherification over alkylation selectivity $S_{B/P}$ increases as the nanosheet thickness increases due to the reduction of the external acid site fraction f_{ext} with nanosheet thickness (Figure 5a). However, this trend does not continue. For larger crystals (points 4, 5 and 6 in Figure 5b), selectivity decreases, despite their even lower f_{ext}, due to the onset of diffusion limitations reflected in η_m decrease. As a result, the maximum selectivity that can be obtained with directly-synthesized catalysts before steam treatment at the specific reaction conditions cannot exceed ca. 5. However, as shown in Figure 5b, s-SPP and s-tk-SPP exhibit selectivities of 6.8 and 20.2, respectively, which greatly exceed the selectivities of their parent materials before steam treatment (2.7 and 4.2, respectively). Another SPP catalyst with

10.1002/anie.202000395

Table 1. Effect of steam-induced coarsening on Brønsted acid catalysis by aluminosilicate SPP. Brønsted acid site density, mass-normalized rate of diethyl ether formation from ethanol dehydration, mass-normalized rate of dibenzyl ether formation from benzyl alcohol etherification, mass-normalized rate of 1,3,5-trimethyl-2-benzylbenzene formation from benzyl alcohol alkylation with mesitylene, external Brønsted acid sites' fraction (f_{ext}), half-thickness along the *b*-axis (x_p) and selectivity ($S_{B/P}$) of thin-SPP (SPP), steamed-thin-SPP (s-SPP), thick-SPP (tk-SPP) and steamed-thick-SPP (s-tk-SPP) materials.

Material	Brønsted acid site density[a] [µmol g^{-1}]	Initial rate of diethyl ether formation [µmol g^{-1} min^{-1}]	Rate of dibenzyl ether formation [µmol L^{-1} s^{-1} g^{-1}]	Rate of 1,3,5-trimethyl-2-benzylbenzene formation [µmol L^{-1} s^{-1} g^{-1}]	f_{ext}[b] [%]	x_p[c] [nm]	$S_{B/P}$[d]
SPP	135	26.0	15.6	5.8	47	1.9	2.7
s-SPP	106	15.3	9.7	1.4	51	3.8	6.8
tk-SPP	158	26.1	13.1	3.1	21	3.7	4.2
s-tk-SPP	133	22.6	7.6	0.4	27	4.6	20.2

[a] Determined by Hofmann elimination of *tert*-butyl amine via reactive gas chromatography.[47] [b] Determined by ethanol dehydration using 2,6-di-*tert*-butylpyridine (DTBP) as a titrant of the external Brønsted acid sites.[48] f_{ext} = (1 – ((rate of diethyl ether formation with DTBP after saturation)/(steady state rate of diethyl ether formation without DTBP))) x 100 %. [c] Determined using TEM for one hundred MFI domains and corresponds to the average of the half-thickness along the *b*-axis of the nanosheets. [d] Determined as the ratio of dibenzyl ether formation rate at 5 % conversion of benzyl alcohol by 1,3,5-trimethyl-2-benzylbenzene formation rate at 5 % conversion of benzyl alcohol.[37]

intermediate nanosheet thickness (i-SPP) is also included in Figure 5b and follows a similar trend with the selectivity increasing from 4.0 to 8.6 after steam treatment. This significant increase in selectivity upon steam treatment is due to the 75 % to 90 % reduction in alkylation mass-normalized rate, while the decrease in the rate of etherification ranges from 38 % to 42 % (Table 1). Part of these losses in catalytic activity (up to 25 %) can be attributed to the overall reduction in the acid site concentration as determined by the Hofmann elimination of *tert*-butylamine. The activity losses for alkylation greatly exceed 25 % and can only be attributed to loss of external (mesopore) catalytic activity since this reaction only takes place on the external surface of the nanosheets. Similar loss of external catalytic activity should also be experienced for the etherification rate. However, based on a model developed earlier,[37] the major fraction (ca. 75 %) of etherification reaction is being contributed by catalysis in the micropores even for the thinnest nanosheets; therefore, the overall (due to external and micropore acid sites) etherification rate does not decrease as much as the alkylation rate.

What causes the large reduction of catalytic alkylation rates on the external surface of nanosheets upon their steam-induced coarsening, given that the nature of active sites remains unaltered as probed by the ethanol dehydration to diethyl ether in the absence of DTBP (Table S3) and confirmed by the results of infrared (IR) spectroscopy using pyridine as a base probe shown in Figure S7? In our earlier work, we demonstrated that the alkylation rate constant depends strongly on the structure of the external surface of the zeolite by quantifying a 10-fold increase in alkylation rate on MWW nanosheets compared to that on the surface of MFI nanosheets.[37] It is plausible that the reduced abundance of (010) faces and their replacement with other not well-defined facets create topologically and chemically distinct environments around the external acid sites that although do not affect the catalytic activity for reactions like ethanol dehydration, they compromise it for reactions involving larger and less polar molecules like mesitylene. The rough facets of the coarsened external surfaces of the steamed catalysts may have affected the accommodation of mesitylene and probably the stabilization of the bulky transition state of the alkylation reaction resulting in reduced rates.

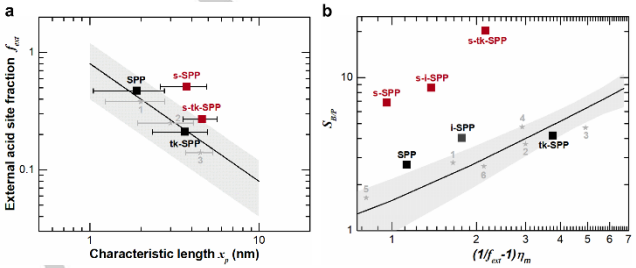

Figure 5. Effect of steam-induced coarsening on Brønsted acid catalysis by aluminosilicate SPP. a) Fraction of external Brønsted acid sites of thin-SPP (SPP; black), steamed-thin-SPP (s-SPP; red), thick-SPP (tk-SPP; black) and steamed-thick-SPP (s-tk-SPP; red) zeolites (f_{ext}) determined by ethanol dehydration using 2,6-di-*tert*-butylpyridine (DTBP)[48] as a function of the characteristic diffusion length corresponding to the nanosheet half-thickness along the *b*-axis (x_p) as determined by TEM for one hundred MFI domains. 1, 2 and 3 correspond to previously reported[37] SPP (without steam treatment) with x_p = 2 ± 1 nm, x_p = 3 ± 1 and x_p = 4 ± 1 nm, respectively. Error bars represent the standard deviation of the mean of measured x_p. The solid straight line (black) corresponds to the geometric model developed earlier[37] for high-aspect-ratio nanosheets: $f_{ext} = d/x_p$, where d = 0.8 ± 0.4 nm (the accessible thickness by DTBP assuming that the Brønsted acid sites are randomly distributed). The grey region represents the error in the determination of the fraction of external Brønsted acid sites resulting from the error in the accessible thickness by DTBP. b) Selectivity ($S_{B/P}$) (etherification rate over alkylation rate) as a function of the external acid site fraction (f_{ext}) and the effectiveness factor (η_m) of thin-SPP (SPP; black), steamed-thin-SPP (s-SPP; red), thick-SPP (tk-SPP; black), steamed-thick-SPP (s-tk-SPP; red), SPP with intermediate nanosheet thickness before (i-SPP; black) and after steam treatment (s-i-SPP; red) zeolites. 1, 2 and 3 are the same as those in Figure 5a and 4, 5 and 6 correspond[35,37] to calcined untreated conventional MFI zeolites with a nominal particle size of 0.2 µm, 1.4 µm and 17 µm, respectively. The solid line (black) corresponds to the selectivity ($S_{B/P}$) expression developed earlier[37] and given in Eq. S4. The grey region represents the error in the selectivity determination resulting from the 95 % confidence intervals of the estimated modeled parameters listed in Table S2.[37]

Conclusion

Steam-induced coarsening of single-unit-cell nanosheets reduces the external surface catalytic alkylation rates while maintains kinetically-controlled micropore etherification catalysis unaltered. This finding is of practical significance as it provides a new method to regulate external surface catalytic activity while preserving micropore reaction rates in zeolite nanosheets, for which, due to their nm-thickness, conventional approaches, like

aluminum-zoning, are difficult to implement. Of fundamental significance is that aluminosilicate MFI nanosheets catalysts can exhibit external surface structure sensitivity, e.g., with (010) facets being more reactive than coarser MFI surfaces, for certain reactions. Electron microscopy proves to be the necessary characterization method to link these pronounced catalytic performance changes to nanoscale coarsening. Data from other characterization techniques, including porosimetry, XRD and NMR remain invariant, while probe reactions like Hofmann elimination of *tert*-butylamine and ethanol dehydration in the absence and presence of DTBP do not exhibit external surface structure sensitivity.

Acknowledgements

This work was supported by the Catalysis Center for Energy Innovation, an Energy Frontier Research Center funded by the U.S. Department of Energy, Office of Science, Basic Energy Sciences under Award DE-SC0001004; and, in its earlier stages, by ADMIRE (Abu Dhabi–Minnesota Institute for Research Excellence) through the Petroleum Institute (now Khalifa University of Science and Technology). Parts of this work were carried out in the Characterization Facility, University of Minnesota, which receives partial support from NSF through the MRSEC program. Y.G. acknowledges support from ADNOC (Abu Dhabi National Oil Company). We thank Dr. S. Hwang (Caltech) for performing the solid-state NMR experiments.

Keywords: catalysis • electron tomography • stability • two dimensional materials • zeolites

[1] B. Elyassi, X. Zhang, M. Tsapatsis, *Microporous Mesoporous Mater.* **2014**, *193*, 134–144.
[2] S. van Donk, A. H. Janssen, J. H. Bitter, K. P. de Jong, *Catal. Rev.* **2003**, *45*, 297–319.
[3] T. Ennaert, J. Geboers, E. Gobechiya, C. M. Courtin, M. Kurttepeli, K. Houthoofd, C. E. A. Kirschhock, P. C. M. M. Magusin, S. Bals, P. A. Jacobs, et al., *ACS Catal.* **2015**, *5*, 754–768.
[4] A. Vjunov, J. L. Fulton, D. M. Camaioni, J. Z. Hu, S. D. Burton, I. Arslan, J. A. Lercher, *Chem. Mater.* **2015**, *27*, 3533–3545.
[5] K. Chen, J. Kelsey, J. L. White, L. Zhang, D. Resasco, *ACS Catal.* **2015**, *5*, 7480–7487.
[6] L. R. Aramburo, L. Karwacki, P. Cubillas, S. Asahina, D. A. M. de Winter, M. R. Drury, I. L. C. Buurmans, E. Stavitski, D. Mores, M. Daturi, et al., *Chem. A Eur. J.* **2011**, *17*, 13773–13781.
[7] M. C. Silaghi, C. Chizallet, P. Raybaud, *Microporous Mesoporous Mater.* **2014**, *191*, 82–96.
[8] L. Karwacki, D. A. M. de Winter, L. R. Aramburo, M. N. Lebbink, J. A. Post, M. R. Drury, B. M. Weckhuysen, *Angew. Chemie Int. Ed.* **2011**, *50*, 1294–1298.
[9] D. Mehlhorn, R. Valiullin, J. Kärger, K. Cho, R. Ryoo, *Microporous Mesoporous Mater.* **2012**, *164*, 273–279.
[10] L. R. Aramburo, Y. Liu, T. Tyliszczak, F. M. F. de Groot, J. C. Andrews, B. M. Weckhuysen, *ChemPhysChem* **2013**, *14*, 496–499.
[11] S. M. T. Almutairi, B. Mezari, E. A. Pidko, P. C. M. M. Magusin, E. J. M. Hensen, *J. Catal.* **2013**, *307*, 194–203.
[12] M. Milina, S. Mitchell, N. L. Michels, J. Kenvin, J. Pérez-Ramírez, *J. Catal.* **2013**, *308*, 398–407.
[13] L. Zhang, K. Chen, B. Chen, J. L. White, D. E. Resasco, *J. Am. Chem. Soc.* **2015**, *137*, 11810–11819.
[14] R. M. Ravenelle, F. Schüßler, A. D'Amico, N. Danilina, J. A. van Bokhoven, J. A. Lercher, C. W. Jones, C. Sievers, *J. Phys. Chem. C* **2010**, *114*, 19582–19595.
[15] G. T. Kerr, *J. Phys. Chem.* **1967**, *71*, 4155–4156.
[16] C. J. Heard, L. Grajciar, C. M. Rice, S. M. Pugh, P. Nachtigall, S. E. Ashbrook, R. E. Morris, *Nat. Commun.* **2019**, *10*, 4690.
[17] S. Malola, S. Svelle, F. L. Bleken, O. Swang, *Angew. Chemie Int. Ed.* **2012**, *51*, 652–655.
[18] M. C. Silaghi, C. Chizallet, E. Petracovschi, T. Kerber, J. Sauer, P. Raybaud, *ACS Catal.* **2015**, *5*, 11–15.
[19] R. Gounder, A. J. Jones, R. T. Carr, E. Iglesia, *J. Catal.* **2012**, *286*, 214–223.
[20] L. R. Aramburo, J. Ruiz-Martínez, J. P. Hofmann, B. M. Weckhuysen, *Catal. Sci. Technol.* **2013**, *3*, 1208–1214.
[21] L. R. Aramburo, E. de Smit, B. Arstad, M. M. van Schooneveld, L. Sommer, A. Juhin, T. Yokosawa, H. W. Zandbergen, U. Olsbye, F. M. F. de Groot, et al., *Angew. Chemie Int. Ed.* **2012**, *51*, 3616–3619.
[22] D. E. Perea, I. Arslan, J. Liu, Z. Ristanović, L. Kovarik, B. W. Arey, J. A. Lercher, S. R. Bare, B. M. Weckhuysen, *Nat. Commun.* **2015**, *6*, 7589.
[23] C. A. Fyfe, J. L. Bretherton, L. Y. Lam, *J. Am. Chem. Soc.* **2001**, *123*, 5285–5291.
[24] M. Choi, K. Na, J. Kim, Y. Sakamoto, O. Terasaki, R. Ryoo, *Nature* **2009**, *461*, 246–249.
[25] K. Kim, R. Ryoo, H. D. Jang, M. Choi, *J. Catal.* **2012**, *288*, 115–123.
[26] W. J. Roth, P. Nachtigall, R. E. Morris, J. Čejka, *Chem. Rev.* **2014**, *114*, 4807–4837.
[27] M. E. Davis, *Nature* **2002**, *417*, 813–821.
[28] M. A. Snyder, M. Tsapatsis, *Angew. Chem. Int. Ed* **2007**, *46*, 7560–7573.
[29] C. M. Lew, R. Cai, Y. Yan, *Acc. Chem. Res.* **2009**, *43*, 210–219.
[30] M. V. Opanasenko, W. J. Roth, J. Čejka, *Catal. Sci. Technol.* **2016**, *6*, 2467–2484.
[31] M. Hartmann, A. G. Machoke, W. Schwieger, *Chem. Soc. Rev.* **2016**, *45*, 3313–3330.
[32] M. S. Holm, E. Taarning, K. Egeblad, C. H. Christensen, *Catal. Today* **2011**, *168*, 3–16.
[33] J. Pérez-Ramírez, C. H. Christensen, K. Egeblad, C. H. Christensen, J. C. Groen, *Chem. Soc. Rev.* **2008**, *37*, 2530–2542.
[34] L. H. Chen, X. Y. Li, J. C. Rooke, Y. H. Zhang, X. Y. Yang, Y. Tang, F. S. Xiao, B. L. Su, *J. Mater. Chem.* **2012**, *22*, 17381–17403.
[35] X. Zhang, D. Liu, D. Xu, S. Asahina, K. A. Cychosz, K. V. Agrawal, Y. Al Wahedi, A. Bhan, S. Al Hashimi, O. Terasaki, M. Thommes, M. Tsapatsis, *Science* **2012**, *336*, 1684–1687.
[36] D. Xu, G. R. Swindlehurst, H. Wu, D. H. Olson, X. Zhang, M. Tsapatsis, *Adv. Funct. Mater.* **2014**, *24*, 201–208.
[37] D. Xu, O. Abdelrahman, S. Hyun Ahn, Y. Guefrachi, A. Kuznetsov, L. Ren, S. Hwang, M. Khaleel, S. Al Hassan, D. Liu, et al., *AIChE J* **2019**, *65*, 1067–1075.
[38] L. Ren, Q. Guo, P. Kumar, M. Orazov, D. Xu, S. M. Alhassan, K. A. Mkhoyan, M. E. Davis, M. Tsapatsis, *Angew. Chemie Int. Ed.* **2015**, *54*, 10848–10851.
[39] P. A. Midgley, R. E. Dunin-Borkowski, *Nat. Mater.* **2009**, *8*, 271–280.
[40] H. Friedrich, P. E. de Jongh, A. J. Verkleij, K. P. de Jong, *Chem. Rev.* **2009**, *109*, 1613–1629.
[41] Y. Wei, T. E. Parmentier, K. P. de Jong, J. Zečević, *Chem. Soc. Rev.* **2015**, *44*, 7234–61.
[42] J. R. Kremer, D. N. Mastronarde, J. R. McIntosh, *J. Struct. Biol.* **1996**, *116*, 71–76.
[43] A. Zecchina, S. Bordiga, G. Spoto, L. Marchese, G. Petrini, G. Leofanti, M. Padovan, *J. Phys. Chem.* **1992**, *96*, 4991–4997.
[44] V. Nikolakis, M. Tsapatsis, D. G. Vlachos, *Langmuir* **2003**, *19*, 4619–4626.
[45] P. M. Piccione, C. Laberty, S. Yang, M. A. Camblor, A. Navrotsky, M. E. Davis, *J. Phys. Chem. B* **2000**, *104*, 10001–10011.
[46] J. D. Rimer, O. Trofymluk, A. Navrotsky, R. F. Lobo, D. G. Vlachos, *Chem. Mater.* **2007**, *19*, 4189–4197.
[47] O. A. Abdelrahman, K. P. Vinter, L. Ren, D. Xu, R. J. Gorte, M. Tsapatsis, P. J. Dauenhauer, *Catal. Sci. Technol.* **2017**, *7*, 3831–3841.
[48] D. Liu, A. Bhan, M. Tsapatsis, S. Al Hashimi, *ACS Catal.* **2011**, *1*, 7–17.
[49] A. Corma, V. Fornés, L. Forni, F. Márquez, J. Martínez-Triguero, D. Moscotti, *J. Catal.* **1998**, *179*, 451–458.
[50] K. Góragóra-Marek, K. Tarach, M. Choi, *J. Phys. Chem. C* **2014**, *118*, 12266–12274.

10.1002/anie.202000395

[51] D. Liu, X. Zhang, A. Bhan, M. Tsapatsis, *Microporous Mesoporous Mater.* **2014**, *200*, 287–290.
[52] A. Korde, B. Min, Q. Almas, Y. Chiang, S. Nair, C. W. Jones, *ChemCatChem* **2019**, *11*, 4548–4557.

10.1002/anie.202000395

WILEY-VCH

RESEARCH ARTICLE

Entry for the Table of Contents

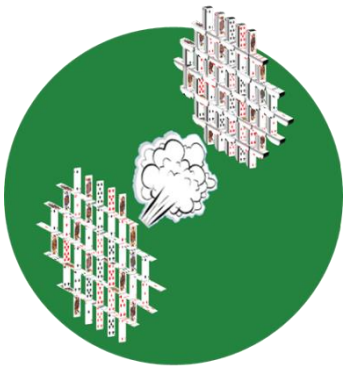

A two-dimensional zeolite undergoes pronounced steam-induced coarsening detectable only by electron microscopy, while it evades detection by commonly used diffraction, porosimetry and catalytic probe reaction methods. For a reaction involving bulky molecules, the observed coarsening remarkably alters external surface catalytic activity, while preserving microporous catalysis unaltered, demonstrating a new method to fine-tune selectivity.